Indoor Tracking of Multiple Individuals With an 802.11ax Wi-Fi-Based Multi-Antenna Passive Radar

Laurent Storrer, *Member, IEEE*, Hasan Can Yildirim, *Member, IEEE*, Morgane Crauwels, Evert I. Pocoma Copa, Sofie Pollin, *Senior Member, IEEE*, Jérôme Louveaux, *Member, IEEE*, Philippe De Doncker, *Member, IEEE*, and François Horlin, *Member, IEEE*

***Abstract*—We investigate indoor human multi-target tracking in cartesian coordinates based on range, Doppler and Angle-of-Arrival measurements obtained with a four-antenna passive bistatic radar capturing 802.11ax Wi-Fi signals. A reference antenna selection method is described to perform angle processing correctly when dealing with target detection diversity among antennas. The tracking is performed by an Unscented Kalman Filter (UKF) to handle the non-linear relation between the measurement space and the state space. A Joint Probabilistic Data Association Filter is coupled to the UKF to handle the data association between tracks and measurements when dealing with multiple targets. Simulations are performed to determine the tracking parameters under heavy constraints and identify key scenarios. An experimental setup is built using Universal Software Radio Peripherals, featuring an over-the-air phase calibration for angle processing with an anchor antenna. It is used to validate the proposed single and multi-target tracking scheme.**

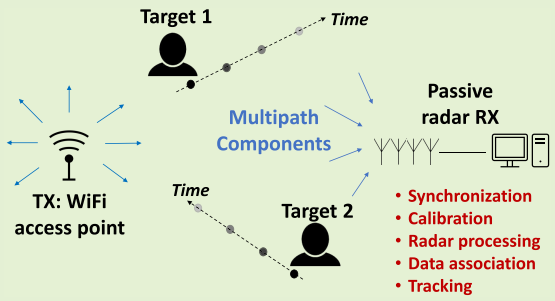

***Index Terms*— Joint probabilistic data association filter, multi-antenna, passive radar, tracking, unscented Kalman filter, Wi-Fi, 802.11ax.**

I. Introduction

Wi-Fi-BASED remote monitoring has drawn increasing attention since the creation of the Task Group for WLAN Sensing [1]. One of the main goals is to detect the presence of objects or human targets in an environment, along with some of their features such as range, speed, and angle with respect to the sensor. Potential applications include human and vehicular target tracking [2], movement classification [3], and non-intrusive area monitoring methods [4].

Remote monitoring can be achieved through a Wi-Fi-based passive bistatic radar (PBR). Radars use multipath components (MPCs) bouncing on the targets of interest to deduce their distance based on the propagation time (*range processing*), their speed based on the Doppler effect (*speed processing*), and their angle w.r.t. the radar if it is equipped with multiple reception antennas (*angle processing*). In the case of passive bistatic radars, the transmitter TX is a non-cooperative source of opportunity, not colocated with the receiver RX. Due to their quasi-ubiquitous availability, Wi-Fi signals are an adequate source of opportunity. Furthermore, they resort to the Orthogonal Frequency Division Multiplexing (OFDM) modulation that is convenient for radar processing. Therefore, a Wi-Fi access point (AP) could be exploited as a transmitter for a Wi-Fi-based PBR. The receiver can be any device equipped with antennas capable of capturing signals at the adequate carrier frequency, *i.e.* in the S-band around 2.45 GHz and in the C-band around 5 GHz [5], and with an appropriate signal acquisition chain.

A single-antenna PBR outputs a so-called range-Doppler map (RDM) or range-speed map, *i.e.* a 2D map where targets are identified by amplitude peaks. It can be obtained by

Manuscript received June 7, 2021; revised July 2, 2021; accepted July 5, 2021. Date of publication July 8, 2021; date of current version September 15, 2021. This work was funded by the Excellence of Science (EOS) Multi-Service Wireless Network Program from the Fonds de la Recherche Scientifique (F.R.S–FNRS) of Belgium. The associate editor coordinating the review of this article and approving it for publication was Prof. Pierluigi Salvo Rossi. *(Corresponding author: Laurent Storrer.)*

Laurent Storrer is with the OPERA Wireless Communication Group (OPERA-WCG), Université Libre de Bruxelles (ULB), 1050 Bruxelles, Belgium, and also with the Department of Electrical Engineering (ESAT), Katholieke Universiteit Leuven (KUL), 3000 Leuven, Belgium (e-mail: laurent.storrer@ulb.be).

Hasan Can Yildirim, Evert I. Pocoma Copa, Philippe De Doncker, and François Horlin are with the OPERA Wireless Communication Group (OPERA-WCG), Université Libre de Bruxelles (ULB), 1050 Bruxelles, Belgium (e-mail: hasan.can.yildirim@ulb.be; epocomac@ulb.be; philippe.dedoncker@ulb.ac.be; fhorlin@ulb.ac.be).

Morgane Crauwels is with the Hubgrade Smart Monitoring Center of Veolia, Brussels, Belgium (e-mail: morgane.crauwels@gmail.com).

Sofie Pollin is with the Department of Electrical Engineering (ESAT), Katholieke Universiteit Leuven (KUL), 3000 Leuven, Belgium (e-mail: sofie.pollin@kuleuven.be).

Jérôme Louveaux is with the Institute of Information and Communication Technologies, Electronics and Applied Mathematics (ICTEAM), Université Catholique de Louvain (UCL), 1348 Ottignies-Louvain-la-Neuve, Belgium (e-mail: jerome.louveaux@uclouvain.be).

Digital Object Identifier 10.1109/JSEN.2021.3095675

performing the range and speed processing simultaneously via a 2D cross-correlation function [2] or in a decoupled fashion by processing separately the range and the speed with channel estimation and a Fast Fourier Transform (FFT) over the Doppler dimension [6]. The knowledge of the transmitted signal is required for both approaches. It can be acquired by pointing a highly directive antenna towards TX, following a so-called reference channel approach [2]. A method requiring fewer resources is to use the known training fields at the beginning of each Wi-Fi packet [5], [7] [8]. A multi-antenna PBR also allows one to exploit the phase difference in the received signal between antennas to compute the angle-of-arrival (AoA) of the MPCs corresponding to targets and typically outputs a so-called range-Doppler-angle cube (RDAC) [8].

One of the main interests of the PBR approach is to use the range-speed or range-speed-angle measurements to perform localization and tracking in an *x-y* coordinates system for movement monitoring. There are mainly three options to achieve this: i. using a multistatic passive radar with range-speed only measurement, *i.e.* featuring several receivers, ii. using a bistatic passive radar with multiple antennas with range-speed-angle measurements, or iii. combining both [9].

The first approach is investigated in [10], where the target position is computed either by an iterative positioning algorithm or by performing a separate line tracking in the range-Doppler space with a standard Kalman Filter and intersecting the two obtained bistatic ellipses.

A comparison of the three approaches is presented in [9] to track a car movement outdoors. The authors use a setup based on a former version of the 802.11 Wi-Fi standard and consisting of a multistatic radar with two receivers, including one receiver with two antennas for angle computation. They demonstrate that using an angle measurement is critical for precise target tracking in Cartesian coordinates. The two best approaches are shown to be the third approach mentioned hereabove (combining the multistatic radar with angle measurement) using a maximum-likelihood position estimate and the second approach (bistatic approach with angle measurement) by intersecting the bistatic ellipse given by the range and the line yielded by the angle.

In [11], the authors show that it is also possible to perform tracking with Doppler-only measurements collected by a multistatic passive radar. They resort to an Extended Kalman Filter to handle the non-linearities in the underlying observation model. Resorting to a particle filter is also an alternative to deal with those non-linearities. The two approaches are validated experimentally on short-range indoor measurements of a single human target.

The importance of being able to track multiple targets with Wi-Fi-based passive radars is also emphasized in [12]. An Unscented Kalman Filter is combined with a Multiple Hypothesis Tracking algorithm to deal with the data association problem in a multi-target scenario. However, it is not validated on experimental measurements. Furthermore, the simulated data rely on a former version of the 802.11 standard with limited bandwidth.

In this paper, we simulate and experimentally demonstrate the feasibility of a Wi-Fi-based PBR for multiple human target tracking based on the latest Wi-Fi standard, 802.11ax. The progress compared to the state-of-the-art presented hereabove is the following:

- Our multiple targets tracking scheme is validated experimentally on human targets, and with targets moving close to each other;
- The tracking takes place indoors, yet still on long distances. It thus has to deal with a low target-SNR of the true target compared to the target-SNR of ghost targets and other MPCs inherent to the indoor environment. The target-SNR is here defined as the ratio between the target peak power and the noise floor in the RDAC;
- We resort to the latest Wi-Fi standard, 802.11ax, leveraging the increased 80 MHz signal bandwidth for better range resolution compared to previous versions of the standard [5];
- We demonstrate that the sole use of the known 802.11ax Preamble field provides sufficient accuracy for tracking, therefore getting rid of the need for a reference channel;
- We use only one 4-antenna Uniform Linear Array receiver built with Universal Software Radio Peripherals (USRPs) calibrated over-the-air to cancel hardware-induced parasitic phase shifts, based on our previous work on the matter [8]. We propose a novel method for reference antenna selection when antenna face detection or synchronization differences. Therefore we do not resort to a multistatic PBR configuration.
- We provide a detailed procedure to perform the tuning of the tracking filter to deal with the heavy constraints imposed by the Wi-Fi-based PBR.

This article is structured as follows: in Section II, the system model is summarized. Section III presents the associated radar processing. In Section IV the data association and tracking schemes are presented. Section V explains the main system constraints, the challenges to handle as well as the scenarios investigated in simulations and measurements. Section VI presents the simulation results used to tune the parameters of the tracking algorithm and the simulation of a large-scale scenario. Finally, Section VII contains the experimental setup and measurement results. As a convention, bold lowercase letters correspond to vectors, matrices, or tensors of time-domain signals (*e.g.* $\boldsymbol{s}$). Similarly, bold uppercase letters correspond to vector, matrices, or tensors of frequency-domain signals (*e.g.* $\boldsymbol{S}$). Calligraphic uppercase letters correspond to sets (*e.g.* $\mathcal{Z}$). The symbol $\mathbb{P}$ denotes a probability.

II. System Model

Wi-Fi signals are considered to be transmitted in bursts of packets. Each burst contains N packets, and the time between the beginning of each burst is T_p. The first OFDM symbol of each packet is a fully 802.11ax-compliant High Efficiency-Long Training Field (HE-LTF) [5]. In each packet, the HE-LTF is followed by κ unknown data symbols. This replicates the behaviour of Wi-Fi transmissions where only the training OFDM symbols at the beginning of a packet are known and usable for radar processing. Each OFDM

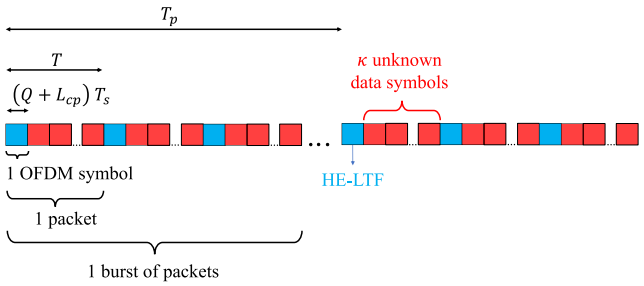

Fig. 1. Symbols, packets and bursts.

symbol, including the HE-LTF, contains $Q + L_{cp}$ samples for a duration $(Q + L_{cp})T_s$, with $T_s = 1/B$ the sampling time, B the bandwidth, Q the number of OFDM subcarriers and L_{cp} the length of the Cyclic Prefix. The sampling time T_s is also referred to as the *fast time*, and the corresponding discrete-time instants are indexed with the fast time index $i = 0, \ldots, Q-1$. The time between the reception of two HE-LTFs is given by $T = (\kappa+1)(Q+L_{cp})T_s$. This duration is referred to as *slow time*, and indexed with the slow time index $k = 0, 1, \ldots, N-1$. These elements are illustrated in Fig. 1.

The environment containing targets and static objects is modelled by a channel transfer function (CTF) and its corresponding channel impulse response (CIR) in the time domain. The CTF varies between the reception of each HE-LTF symbol, *i.e.* with the slow time, due to the phase changes induced by the Doppler shifts of the targets. There is also one CTF per RX antenna, indicated with index $l = 0, 1, \ldots, L-1$ where L is the number of RX antennas. Upon reception of an HE-LTF, the CTF is estimated on each of the $q = -Q/2, \ldots, Q/2-1$ subcarriers of the OFDM spectrum. For one burst of N packets, the CTFs can thus be represented by a 3D tensor $\boldsymbol{H}$ whose elements are [13]

$$\boldsymbol{H}[q,k,l] = \sum_{r=0}^{N_r} \alpha_r \; e^{-j2\pi f_c \tau_r} \; e^{j2\pi l \Delta \sin(\theta_r) + j\Phi_l} \; e^{j2\pi f_r k T} \; e^{j2\pi \frac{q}{Q} B \tau_r} \; \text{rect}\left(\frac{q}{Q}\right), \quad (1)$$

where the index r denotes each of the N_r objects or targets in the environment, considering only the corresponding first-order reflection MPC (single bounce model). For each target, this MPC is characterized by:

- Its propagation delay τ_r to the first antenna of the RX array, corresponding to the bistatic distance $d_r = d_{\text{TX-target}} + d_{\text{target-RX}}$. It is linked to a fast time index $i_r = \lfloor \tau_r / T_s \rceil$ and a bistatic distance $\hat{d}_r = i_r T_s c$, with c the speed of light in vacuum.
- Its Doppler frequency shift $f_r = \frac{2v_r}{\lambda}\varepsilon_r$, where v_r is the target speed, λ is the wavelength and $-1 \leq \varepsilon \leq 1$ is a projection factor depending on the bistatic geometry, whose absolute value is maximal when the target moves perpendicularly to the baseline TX-RX [14].
- Its AoA θ_r w.r.t. the line perpendicular to the RX antenna array baseline.
- Its complex amplitude α_r.

TABLE I
INDICES, SIGNALS & MPCS FEATURES

Symbol	Name
i	Fast time index
q	Subcarrier index
k	Slow time index
n	Doppler frequency bin
l	Antenna index
p	Tracking time index
r	Target index
r'	Detection index
t	Target track index
$\boldsymbol{H}$	CTF tensor
$\boldsymbol{h}$	CIR tensor
$\boldsymbol{D}$	Range-Doppler-angle cube (RDAC)
$\boldsymbol{D}_r$	RDAC target vector
τ_r	Propagation delay of the r-th MPC
f_r	Doppler frequency of the r-th MPC
v_r	Speed of the r-th MPC
θ_r	Angle-of-arrival of the r-th MPC
α_r	Complex amplitude of the r-th MPC

The index $r = 0$ refers to the direct path between TX and RX. The other indices refer to the objects or targets in the environment. The term f_c is the carrier frequency, and $\Delta = \delta_{ant}/\lambda$ where δ_{ant} is the antenna spacing at RX. The exponential $e^{j2\pi l \Delta \sin(\theta_r)}$ is due to the extra propagation delay of the MPCs between the first antenna and the l-th antenna. It is exploited to estimate the MPCs AoA θ_r. However, this AoA term is affected by an unwanted phase shift Φ_l induced by the hardware acquisition chain of each antenna, that has to be compensated, as explained in Section III. Finally, the $e^{j2\pi \frac{q}{Q} B \tau_r}\text{rect}(q/Q)$ term is due to the sampling with a limited sampling rate. In the time domain, it corresponds to a sinc that creates what we express here as *delay leakage*: when the propagation delay τ_r is not an integer multiple of the sampling time T_s, the energy of the MPC leaks on the neighbouring delay bins. It is a direct consequence of having bandlimited signals [15]. This leaking energy can complicate the target detection and even affect other targets located at other delay bins.

A summary of the different indices, signals and MPCs features is given in Table I.

III. RADAR PROCESSING

Based on the CTF model, the goal of the radar processing is to estimate d_r, v_r and θ_r for each target. This estimation is performed on each burst of N packets, using the HE-LTFs only, and fed to the tracking algorithm presented later. The time interval between updates of the tracking is thus the burst interval T_p introduced in Section II, and indexed with $p = 0, 1, \ldots, P-1$ denoted as *tracking time* index, with P the total number of bursts.

A. Time Synchronization

The first step of the processing is the time synchronization between TX and RX, *i.e.* finding the beginning of the packet at the receiver side. It is achieved by correlating the known

transmitted HE-LTF with the received symbols and finding the maximal correlation value. The fast time index of this value corresponds to the propagation delay of the direct path between TX and RX. RX is placed at a distance smaller than the range resolution $d_{res} = cT_s/2$ from TX in a quasi-monostatic configuration [16]. Hence this direct path can be used as the 0 s propagation delay reference. Samples before the direct path index can thus be discarded. However, time misalignment can occur between antennas due to locking delays in the Pulse Per Second (PPS) signal rising edges used to time-align the local clock associated with each antenna with each other [17]. Therefore, the same target can appear on two different range bins depending on the antenna, with a maximal difference of one range bin. This problem is addressed in Section III-G.

B. Hardware-Induced Phase Calibration

The hardware-induced phase shift Φ_l from (1) has to be compensated for the future angle estimation to work. This consists in setting this phase to the common value of Φ_0 for all antennas. Our technique for this calibration relies on the use of empty subcarriers in the OFDM spectrum and on an anchor antenna. In the 802.11ax standard, the 5 frequency subcarriers at the centre of the spectrum of each OFDM symbol are left empty [5]. A complex exponential, called here *calibration exponential* at one of those subcarriers frequency, $f_{cal} = qB/Q$ for $q \in [-2, 2]$, can thus be transmitted from an *anchor* antenna located in front of RX. At the anchor, this complex exponential is expressed in baseband as $x_{cal}[i] = \exp(j2\pi f_{cal} i T_s)$. Upon reception, it is not affected by the angle term $2\pi l \Delta \sin(\theta_r)$ from (1) since the anchor is located in the far field at an angle of 0° w.r.t. RX. The only phase difference between antennas is thus Φ_l. The calibration exponential is located on one unique subcarrier frequency, hence it can be extracted without any filtering. By going back in time-domain and computing the sample offset between the exponentials at each antenna, the phase difference $\Phi_0 - \Phi_l$ can be estimated and cancelled by multiplying the received signal by the scalar $\exp(j(\Phi_0 - \Phi_l))$. Details about the phase calibration can be found in [8].

C. Range Processing

Range processing is the estimation of d_r. The received signal at antenna l is a convolution of the transmitted signal with the CIR at this time instant. In the frequency domain, this corresponds to a product with the CTF. The relation can be inverted to isolate the CTF by a frequency-domain least-square channel estimation [8], [13] using the known HE-LTFs, yielding an estimate $\hat{\boldsymbol{H}}$ of $\boldsymbol{H}$.

If the Doppler shifts are sufficiently small so that the duration of M subsequent packets is inferior to the channel coherence time, which is the case for human targets, the CTFs can be averaged by groups of M [14]. The number of received packets per burst can thus be rewritten as $N = N'M$, with N' the number of remaining slow time points used later for the Doppler FFT presented later. An IFFT is then computed to obtain the estimated CIR tensor:

$$\hat{\boldsymbol{h}}[i, k', l] = \frac{1}{\sqrt{Q}} \sum_{q=-Q/2}^{Q/2-1} \left(\frac{1}{M} \sum_{k=k'M}^{(k'+1)M-1} \hat{\boldsymbol{H}}[q, k, l] \right) e^{j2\pi qi/Q} \quad (2)$$

$$= \sum_{r=0}^{N_r} \alpha_r \; e^{-j2\pi f_c \tau_r} \; e^{j2\pi l \Delta \sin(\theta_r) + j\Phi_l} \; e^{j2\pi f_r k' MT} \operatorname{sinc}(B(\tau_r - iT_s)) + w_{ik'l}. \quad (3)$$

In (2), the outer sum on q is the IFFT, and the inner sum on k is the averaging operation. The index $k' = 0, 1, \ldots, N' - 1$ is the averaged OFDM symbol index corresponding to the discrete time MT. The Doppler exponential term from (1) becomes thus $e^{j2\pi f_r k' MT} \quad \forall k'$ in (3). The last term $w_{ik'l}$ represents the remaining noise originating from the received samples, after channel estimation, averaging and IFFT.

The estimated CIR tensor $\hat{\boldsymbol{h}}$ contains the estimated delay $\hat{\tau}_r = i_r T_s$ of each MPC r, allowing to compute its bistatic distance $\hat{d}_r = c\hat{\tau}_r$. With the quasi-monostatic configuration, the distance between RX and the target is computed from the single bounce model as $\hat{d}_{\text{target-RX}} \approx \hat{d}_r/2$ [16]. The main source of error on the distance estimation is the limited range resolution due to the sampling time. A correct time synchronization from Section III-A is also critical to obtain the true 0 s propagation delay reference, hence the true 0 m distance reference.

D. Speed Processing

An FFT, called here *Doppler FFT*, can be applied along the second dimension of the estimated CIR tensor $\hat{\boldsymbol{h}}$ to extract the Doppler frequency information [14], yielding a so-called *range-Doppler-angle cube* (RDAC):

$$\hat{\boldsymbol{D}}[i, n, l] = \frac{1}{\sqrt{N'}} \sum_{k'=0}^{N'-1} \hat{\boldsymbol{h}}[i, k', l] e^{-j2\pi kn/N'} \quad (4)$$

where $n = -N'/2, \ldots, N'/2 - 1$ is the Doppler bin index. Each frontal slab of the RDAC, $\hat{\boldsymbol{D}}[:, :, l]$, is one aforementioned range-Doppler-map (RDM), in which targets are identified as amplitude peaks. The corresponding Doppler bin n_r of each target gives its estimated Doppler frequency $\hat{f}_r = n_r f_{res}$, where $f_{res} = 1/(N'MT)$ is the frequency resolution of the Doppler FFT. This allows one to estimate the target speed $\hat{v}_r = \lambda \hat{f}_r/2$. A window is usually applied prior to the Doppler FFT to reduce frequency leakage. The limited speed resolution and the projection factor ε_r are the main sources of error in this estimation. Components with $\hat{v}_r = 0$ are considered as *static clutter* and are removed using *Average Removal* [6].

E. Target Detection

The goal of target detection is to separate the RDM cells containing a target from cells containing noise. It is usually performed by thresholding using a Constant False Alarm Rate (CFAR) detector. However, in this work, a local maxima search on each RDM is preferred to avoid detecting the range and Doppler significant points caused by the leakage

(cf. Sections II and III-D) [8]. In the general case, all targets, denoted with an index r, might not be detected, and ghost targets created by higher-order MPCs can also be detected. Hence detections, *i.e.* detected targets, are denoted with a different index $r' \neq r$.

F. Angle Processing

Angle processing is the estimation of $\theta_{r'}$, relying on the phase difference $2\pi l \Delta sin(\theta_{r'})$ between antennas. It is performed separately for each detection point in the RDAC using MUSIC [18]. Assuming no time-alignment error between antennas, each detection occurs at one unique range tap $i_{r'}$ and frequency bin $n_{r'}$ across antennas, and an $L \times 1$ RDAC target vector is built as follows:

$$\hat{\boldsymbol{D}}_{r'} = \left[\hat{\boldsymbol{D}}[i_{r'}, n_{r'}, 0] \ \ldots \ \hat{\boldsymbol{D}}[i_{r'}, n_{r'}, L-1]\right]^T. \tag{5}$$

It contains the RDAC cells of the detected target across antennas. Vector $\hat{\boldsymbol{D}}_{r'}$ is used as input to MUSIC. The output is the MUSIC angle spectrum $J(\theta)$ whose peaks correspond to the AoA $\theta_{r'}$ of the detected MPC. Inputting only this single vector per target allows benefiting from the FFT gain, helping to detect low reflectivity targets like humans. It also avoids the leakage impact and isolates targets from each other. It does not require MUSIC spectrum peak association with detection since the peaks of each MUSIC spectrum all correspond to one RDAC cell. The precision of the angle estimation depends on the target-SNR and the hardware-induced phase calibration from Section III-B. The calibration is critical since without it the angle estimation is erroneous due to hardware-induced phase shift Φ_l in (1). Errors of a few samples in the sample offset estimation during the calibration result in an angle estimation error of the order of one degree [8]. More details on this discussion and the estimation process are given in [8].

G. Antenna Selection

The target detection points in the RDAC can be different between antennas, for different possible reasons, *e.g.* time misalignment due to the PPS signal as explained in Section III-A or channel variations among antennas (power, delay, Doppler).

This is a problem for the angle processing where a unique detection coordinates pair $(i_{r'}, n_{r'})$ was assumed for (5), and for the range and speed estimation since only one $(i_{r'}, n_{r'})$ pair should be used to determine the range and speed of a detected point. Therefore the system should choose between using the detection coordinates of the first antenna as reference or using separate detection coordinates for each antenna. Since the origin of the detection mismatch is not identifiable, both strategies are considered and the one giving the best MUSIC angle spectrum is kept. More formally, the system has to choose between:

1) using the detection coordinates $i_{r'}$ and $n_{r'}$ from the first antenna as a reference to build the target vector for angle estimation as in (5) and to estimate the range and speed.
2) using the detection coordinates $i_{r'l}$ and $n_{r'l}$ separately per antenna l to build a target vector

$$\hat{\boldsymbol{D}}_{r'} = \left[\hat{\boldsymbol{D}}[i_{r'0}, n_{r'0}, 0] \ldots \ \hat{\boldsymbol{D}}[i_{r'(L-1)}, n_{r'(L-1)}, L-1]\right]^T \tag{6}$$

for angle estimation, and choose which $(i_{r'l}, n_{r'l})$ pair to use for the range and speed estimation through a majority voting between antennas, *i.e.* by selecting the final $i_{r'}$ and $n_{r'}$ respectively as the sample mode (most frequently occurring value) of the set $\{i_{r'l} | l = 0, \ldots, L-1\}$ and the set $\{n_{r'l} | l = 0, \ldots, L-1\}$.

We introduce a simple and interpretable criterion to make that decision: the MUSIC spectrum "dynamic range"

$$\text{DR} = \max(J(\theta)) \ / \ \min(J(\theta)). \tag{7}$$

The MUSIC spectrum and its DR are computed for each approach and the approach yielding the highest DR is chosen as the correct one: indeed, the minimum of the MUSIC angle spectrum is the estimation noise floor, and the maximum of the spectrum is the value corresponding to the target AoA. Hence the DR is the ratio between the target peak and the estimation noise floor. The bigger the DR the higher the target peak stands above this noise floor, giving a direct metric of the quality of the angle estimation and allowing to choose the best approach.

Choosing the wrong approach would result in feeding an RDAC target vector $\hat{\boldsymbol{D}}_{r'}$ whose L elements do not all correspond to the r'-th detection across the L antennas, yielding a perturbated MUSIC spectrum for the detected target.

This antenna selection procedure is repeated separately for each detection point r'.

IV. Data Association and Tracking

A. Unscented Kalman Filter

After the radar processing, the collected measurements are transferred to the tracking stage to estimate the target state in Cartesian coordinates based on the measurements and a kinematic model. The tracking filter chosen here is an Unscented Kalman Filter (UKF) [19], to deal with the non-linearities of the measurement model. The goal of the tracking is to estimate the x-y position of the target over time. The state vector $\boldsymbol{x}$ to track comprises the x-y positions but also the speeds for increased precision, and the measurement vector $\boldsymbol{z}$ received for each detection at each tracking time comprises the quasi-monostatic range, speed and AoA estimated by the radar processing:

$$\boldsymbol{x} = [x \ \dot{x} \ y \ \dot{y}]^T \qquad \boldsymbol{z} = \left[\hat{d}/2 \ \hat{v} \ \hat{\theta}\right]^T. \tag{8}$$

The system model of the UKF is the following:

$$\boldsymbol{x}_p = \boldsymbol{f}(\boldsymbol{x}_{p-1}) + \boldsymbol{n}_x \quad \boldsymbol{z}_p = \boldsymbol{h}(\boldsymbol{x}_p) + \boldsymbol{n}_z \tag{9}$$

where $\boldsymbol{f}$ is the dynamic model characterizing a uniform rectilinear motion [20] and $\boldsymbol{h}$ is the non-linear measurement model characterizing a quasi-static scenario assuming that the receiver is at position $(x = 0, y = 0)$ [21]:

$$\boldsymbol{h}(\boldsymbol{x}) = \left[\sqrt{x^2 + y^2} \ \ \frac{x\dot{x} + y\dot{y}}{\sqrt{x^2 + y^2}} \ \ \arctan(x/y)\right]^T. \tag{10}$$

A higher-order model including acceleration in the state space is not chosen here due to the limited information provided by the measurements. As commonly done in the literature, the acceleration is rather assumed to be the source of errors in the model through the error term $\boldsymbol{n}_x$ which represents the difference between the target movement and a true uniform rectilinear motion [20]. It is assumed to be a Gaussian random variable with a covariance matrix

$$\boldsymbol{q} = \begin{bmatrix} T_p^4/4 & T_p^3/2 & 0 & 0 \\ T_p^3/2 & T_p^2 & 0 & 0 \\ 0 & 0 & T_p^4/4 & T_p^3/2 \\ 0 & 0 & T_p^3/2 & T_p^2 \end{bmatrix} \sigma_a^2, \tag{11}$$

following a piecewise white noise model [20], where σ_a^2 is the variance of the acceleration. The term $\boldsymbol{n}_z$ is the classical measurement error term, also modelled as a Gaussian random variable with a 3×3 diagonal covariance matrix whose diagonal consists in the variance σ_d^2, σ_v^2 and σ_θ^2 of the measurement errors on the range, speed and AoA respectively. It is denoted as

$$\boldsymbol{r} = \text{diag}(\sigma_d^2, \sigma_v^2, \sigma_\theta^2). \tag{12}$$

The parameter σ_a represents the uncertainty in the model and the parameters σ_d, σ_v and σ_θ represent the uncertainties in the measurement. The ratio between σ_a and $(\sigma_d, \sigma_v, \sigma_\theta)$ is critical for a correct UKF performance and is tuned according to the Wi-Fi-based PBR constraints in Section VI.

B. State Initialization

The first range-Doppler-angle measurement is used to initiate the Cartesian state. The x and y coordinates are initialized as follows (the subscripts r' are removed for readability):

$$\begin{cases} x = \dfrac{\hat{d}}{2}\sin(\hat{\theta}) \\ y = \dfrac{\hat{d}}{2}\cos(\hat{\theta}) \end{cases} \tag{13}$$

The $\dot{x}$ and $\dot{y}$ speeds can be initialized as 0 m/s, or by inverting the second equation of the measurement model, *i.e.* the second element of the vector in (10):

$$\hat{v} = \frac{x\dot{x} + y\dot{y}}{\sqrt{x^2 + y^2}} = \frac{x\dot{x} + y\dot{y}}{\hat{d}/2} \Leftrightarrow \begin{cases} \dot{x} = \dfrac{\hat{v}\hat{d}/2 - y\dot{y}}{x} \\ \dot{y} = \dfrac{\hat{v}\hat{d}/2 - x\dot{x}}{y} \end{cases} \tag{14}$$

If prior knowledge on one of the initial speeds $\dot{x}$ or $\dot{y}$ is available, the other speed can be initialized. This is the case in a rectangular corridor for example, where one speed can be initialized to 0 m/s, allowing to derive the other one.

C. Joint Probabilistic Data Association Filter

Since multiple targets have to be tracked simultaneously a data association scheme is implemented. A Joint Probabilistic Data Association Filter (JPDAF) is used to this end [22]. Tracks are used to represent detected targets. A track, denoted with index t, is the set of the predicted and measurement-updated states of the target along time. The JPDAF is a soft association scheme which calculates the association probability $\beta_{r't}$ of each measurement-track pair, *i.e.* $r't$ pair, after the prediction step from the dynamical model $\boldsymbol{f}$ of the UKF, jointly across all the tracks, and computes the UKF innovation of each track based on all the measurements found in a so-called gating region of the track, weighted by their association probability. Hence the UKF coupled to JPDAF becomes a "weighted UKF". The gating region is adjusted by a gating probability parameter P_G, set here to the typical value of $P_G = 0.99$ [23]. Association probabilities are computed using *feasible joint association events*: first, *association events* $A_{r't_{r'}}$ between measurements and tracks are considered, with $t_{r'}$ the index of the track to which measurement r' is associated in the association event under consideration. *Joint association events* $A = \bigcap_{r'} A_{r't_{r'}}$ are then determined, consisting of the association events of all measurements to one of the tracks. Finally, *feasible joint association events* A^* are established, which refine the joint association events by considering that a target can generate at most one measurement and that a measurement can have originated from at most one target [22].

Based on the tracks and the set of measurements $\mathcal{Z} = \{\boldsymbol{z}_{|r'}\} = \left\{\left[\hat{d}_{r'}/2 \;\; \hat{v}_{r'} \;\; \hat{\theta}_{r'}\right]^T\right\}$ from all detections r', the probability of each feasible joint association event is

$$\mathbb{P}(A^*|\mathcal{Z}) = \frac{1}{\gamma}\prod_{r'}\left(\lambda_g^{-1} f_{t_{r'}}(\boldsymbol{z}_{|r'})\right)^{\nu_{r'}} \times \prod_t (P_G P_D^t)^{\delta_t}(1 - P_G P_D^t)^{1-\delta_t}. \tag{15}$$

$f_{t_{r'}}$ is the likelihood of the r'-th measurement originating from the target corresponding to track $t_{r'}$. P_D^t is the probability of detection of track t, decreasing with its distance. λ_g is the assumed mean number of ghost targets. $\nu_{r'}$ is the measurement association indicator, which is equal to one if the measurement r' has been associated in the feasible joint association event under consideration and zero otherwise. Similarly, δ_t is the track association indicator which is equal to one if the track has been associated with a measurement and zero otherwise. γ is a normalization constant [22].

Combining all the feasible joint association events where a precise measurement has been associated with a precise track yields the association probability

$$\beta_{r't} = \sum_{A^*: A_{r't} \in A^*} \mathbb{P}(A^*|\mathcal{Z}). \tag{16}$$

More details on JPDAF are given in [22]. Other techniques are also available such as the Multiple Hypothesis Tracking (MHT) mentioned in Section I [12]. MHT is known to be more efficient than JPDAF but at the cost of an unrealistically increased computation time for the considered application if the tracking should happen in real time [24]. Similar reasoning was applied for the choice of the UKF as tracking filter compared to other methods such as particle filters that are more efficient but more computationally intensive [20].

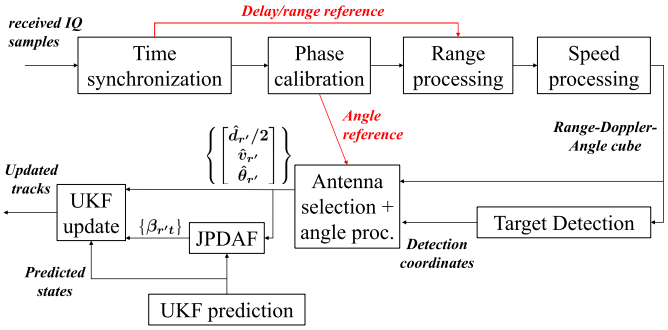

Fig. 2. Radar processing and tracking flowchart.

D. Track Management

For advanced scenarios involving a lot of targets, a track management scheme can be implemented to handle targets appearing or disappearing from the scene. It is also useful to discard false tracks created by ghost targets due to higher-order MPCs.

Track initiation: At a tracking instant p, any measurement that has not been associated with a track is considered as a potential track starting point and produces a *preliminary track*, initiated as described in Section IV-B. A separate tracking is performed on the preliminary tracks. At each tracking instant, the probability of having no measurement associated with the preliminary track, computed by the JPDAF, is compared to a threshold to determine if a measurement was associated with the track [25]. If it is below it constitutes a *hit*, otherwise it is a *miss*. Any miss causes the preliminary track to be discarded. A validation window N_v is chosen: after N_v tracking instants, the remaining preliminary tracks are confirmed as valid tracks. At the first tracking instant $p = 0$, this initiation process is applied on all measurements since no track has been confirmed yet.

Track deletion: a maximal miss number N_{miss} is fixed. If a confirmed track faces N_{miss} misses over subsequent tracking instants, it is deleted [25].

E. Tracking Summary

To sum up, at each tracking instant p, the N packets are received, in which the HE-LTFs are used to perform the radar processing. This produces a set of detections $\mathcal{Z}$ containing the estimated range, speed and angle of each detection r'. In the meantime, the UKF predicts the states of the different tracks t based on their previous values and feeds them to the JPDAF. The JPDAF then exploits the set $\mathcal{Z}$ and the predicted states to produce the set $\mathcal{B} = \{\beta_{r't}\}$ of measurement-track association probabilities. Finally, the sets $\mathcal{Z}$ and $\mathcal{B}$ and the predicted states are fed to the update stage of the UKF which updates the state of each track. Detections not associated with any track can give rise to new tracks, and obsolete tracks can be deleted. The whole radar processing and tracking are summarized in a flowchart in Fig. 2.

V. System Parameters & Scenarios

After the description of the radar processing and tracking techniques, this section lists the limiting parameters of the system, the challenges faced by the tracking, and the different scenarios addressing those challenges.

TABLE II
Parameters

Symbol	Name	Value	Unit
f_c	Carrier frequency	2.45	GHz
B	Signal bandwidth	80	MHz
T_s	Sampling time, *i.e.* fast time	12.5	ns
T	Time between HE-LTFs, *i.e.* slow time	272	μs
T_p	Tracking time	0.5	s
δ_{ant}	Antenna spacing	6	cm
Q	Number of subcarriers	1024	\
L_{cp}	Cyclic Prefix length	64	\
N'	Number of Doppler bins	128	\
M	Number of averaging points	6	\
κ	Number of unknown symbols	19	\
L	Number of antennas	4	\

A. Parameters

The main limiting parameters of the system are:

- The tracking time $T_p = 0.5$ s. This value is chosen to replicate the fact that a Wi-Fi AP does not transmit packets continuously and that a large amount of time can pass between the reception of two bursts of packets, hence between two measurement sets to feed to the tracking filter, compared to traditional active radars as in [26] where the tracking time is of the order of 60 ms. This a heavy constraint that has to be dealt with via proper tracking filter tuning, explained in Section VI-A. Combined with the poor range resolution it gives abrupt jumps in range measurements when the target moves from one range bin to the next. This results in frequent uncertainty jumps in the state covariance matrix of the UKF, degrading the state estimates.
- The bandwidth $B = 80$ MHz from the 802.11ax standard [5]. It gives a coarse range resolution $d_{res} = 1.88$ m. This can give large errors in range estimation and a potential absence of change of range bin of the target between two measurements (*i.e.* between two bursts of packets), causing the UKF to estimate a target speed much lower than the real speed despite the Doppler information.
- The small number of antennas $L = 4$, resulting in a coarse angle resolution. This value is due to the limited parallel data streaming capability of the experimental setup presented in Section VII-A.

The other parameters are summarized in Table II.

B. Challenges

The main challenges of an indoor human multi-target tracking in experimental conditions are the following:

1) Human targets can make abrupt trajectory changes, such as turn arounds, compared to bikes and cars. The challenge is for the JPDAF-UKF to handle the abrupt turn around, *i.e.* to be able to perform a quick change of sign of the estimated $\dot{x}$ or $\dot{y}$. This requires a proper tuning of the UKF parameters, detailed in Section VI-A.
2) The data association, explained and addressed in Section IV-C.
3) Human targets feature a low reflectivity, yielding a low target-SNR, especially at long distances like in corridors,

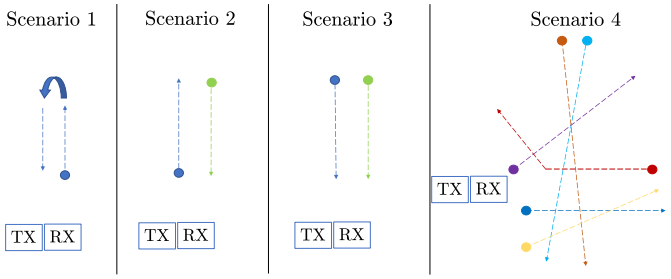

Fig. 3. Illustration of the simulations & measurements scenarios.

lowering the chances of detection and hindering the angle processing which is heavily SNR-dependent. This problem is addressed by resorting to a high digital processing gain with the averaging and the Doppler FFT.

4) As already mentioned, higher-order MPCs due to walls are present, creating so-called ghost targets. Since the tracks formed by ghost targets are not consistent over time, ghost targets are usually cancelled out when the tracking is implemented with track management.

C. Scenarios

Proper tuning of the UKF filter parameters is necessary to deal with the system limits and with the challenges mentioned hereabove. To this end, several typical scenarios are investigated in simulations. Once the filter parameters are determined, the tracking performance in those scenarios is also demonstrated experimentally. The scenarios are the following:

1) **One target with a U-turn:** the first scenario consists of one single human target moving away from the radar along the y-axis, making an abrupt turn around and coming back. This scenario addresses challenge 1).
2) **Two targets with opposite speeds:** the second scenario consists in two targets walking with opposite speeds: the first target is moving away from RX, and the second is moving towards RX. This is a first step to verify the multi-target tracking capability of the proposed scheme and to address challenge 2), because the two targets are well separated in the measurement space since the sign of their Doppler shift is opposite.
3) **Two targets moving side-by-side:** the third scenario is much more challenging. It consists in two targets moving towards the radar side-by-side. This means that both targets are at the same range from the radar and have the same speed. The only difference between them is their angle. Hence, the measurements of the two targets are at a very short distance in the measurement space, pushing the data association to its limits for challenge 2). Furthermore, the targets start far from RX, hence the target-SNRs are low for angle estimation at the beginning of the tracking, addressing challenge 3).

Besides, **a six-target scenario** (scenario 4) is also investigated in simulations, to have a glimpse of how tracking and data association perform for a larger number of targets. All scenarios are illustrated in Fig. 3.

In simulations, the Root Mean Squared Error (RMSE) metric is computed to assess the quality of the position estimation:

$$\text{RMSE} = \sqrt{\frac{1}{N_{real}} \sum_{s=0}^{N_{real}-1} (\hat{x}-x)_s^2 + (\hat{y}-y)_s^2} \tag{17}$$

where N_{real} is the number of realizations of the scenario and the subscript s is the realization index. The value N_{real} is set to 100. With experimental measurements, only one realization is considered, hence with Euclidean distance as performance metric:

$$\text{ED} = \sqrt{(\hat{x}-x)^2 + (\hat{y}-y)^2} \tag{18}$$

VI. Simulations

A. UKF Parameters Tuning

As said previously, for the filter tuning a trade-off has to be found between model uncertainty (σ_a in $\boldsymbol{q}$) and measurement uncertainty ($\sigma_d, \sigma_v, \sigma_\theta$ in $\boldsymbol{r}$). This is why those parameters have to be jointly tuned. The value of σ_a is usually recommended to be set between $\Delta a/2$ and Δa, where Δa is the maximal change of target acceleration that could occur in between two tracking time instants [20]. Here we analyse a broader range of values, between 0.1 and 1.6 m/s^2.

The three parameters of $\boldsymbol{r}$ (σ_d, σ_v and σ_θ) relate directly to radar measurement errors, hence mainly to the radar resolutions on range speed and angle, *i.e.* d_{res}, v_{res} and θ_{res}. This last parameter has not been introduced until now, since there is no analytic formula for angle resolution computed with superresolution methods like MUSIC, except a Cramer-Rao Lower Bound (CRLB) which in this case is too idealized to be close to experimental reality. Based on previous works, an empirical value of $\theta_{res} = 3°$ can be chosen [8], [27]. For fine-tuning, the different resolutions are adjusted by a factor ρ to yield their respective error variance, such that:

$$\boldsymbol{r} = \text{diag}\left(\sigma_d^2, \sigma_v^2, \sigma_\theta^2\right) = \text{diag}\left((d_{res}/\rho)^2, (v_{res}/\rho)^2, (\theta_{res}/\rho)^2\right). \tag{19}$$

Hence this factor becomes the only parameter to tune for the design of $\boldsymbol{r}$ and can be interpreted as a factor of belief in the measurements.

The three first scenarios introduced in Section V-C are simulated by performing a grid search on pairs of σ_a and ρ: for each (σ_a, ρ) pair, noisy measurements from the radar processing are generated at each time instant, including the true target(s), false alarms from noise and ghost targets originating from higher-order MPCs. The tracking is performed assuming a known number of targets, hence a fixed number of tracks, and using all these radar measurements. The RMSE is computed at each time instant. When multiple targets are present, an averaged RMSE is computed with the contribution of each target. The mean on all time instants of the RMSE is also computed and used as the single value representing the quality of the tracking for this (σ_a, ρ) pair. The tested σ_a values range from 0.1 to 1.6 m/s^2, as said above, and the tested values of ρ range from 0.1 to 1.6. Higher values can lead to a divergence of the tracking due to an excessive

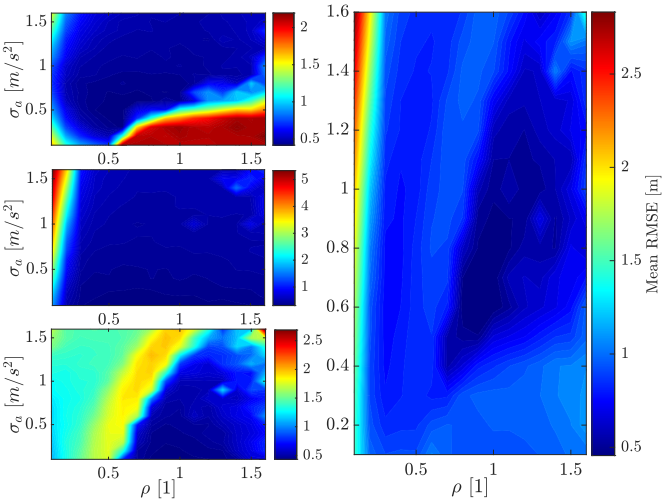

Fig. 4. UKF tuning simulations. Left: mean RMSE in function of σ_a and ρ for Scenario 1 (top), Scenario 2 (middle), Scenario 3 (bottom). Right: mean RMSE averaged on the three scenarios in function of σ_a and ρ.

misbelief in the model (through σ_a) or an unreasonably large belief in measurements (through ρ). The step between tested values is 0.1. A heatmap is generated with the values of mean RMSE for each (σ_a, ρ) pair, and the pair yielding the lowest mean RMSE is selected.

In Scenario 1 the turn around of the target happens at 10 s. It has to be properly handled by the tracking. In Scenario 2, target 1 starts at position $(-1.4, 3)$ m and speed $(0, 1.2)$ m/s, and target 2 starts at position $(1.4, 20)$ m and speed $(0, -1.2)$ m/s. In Scenario 3 the two targets start at $(-1.4, 23)$ m and $(1.4, 23)$ m respectively, at the same speed $(0, -1.2)$ m/s. In this case, the detection points are close to each other in the measurement space, they will thus yield similar JPDAF weights for each target. Hence, each target influences the other. A correct tracking should thus prevent the two tracks to mix. Tracks mixing would be noticed by an increased RMSE.

The resulting RMSE heatmaps for the different scenarios are displayed in the left of Fig. 4. For scenario 1 (top left plot), it can be noticed that a high belief in the model (small σ_a) combined with a high belief in the measurements (high ρ) does not handle the turn around because the filter cannot choose whether it should trust the model or the measurement when the turn around occurs, hence yielding a high RMSE. For scenario 2 (middle left plot), combining a low belief both in the model (high σ_a) and in the measurements (low ρ) is not recommended as it causes tracks to mix when the targets cross each other and RMSE to increase, since at that moment the corresponding measurements are close to each other in the measurement space. This is confirmed by the red zone in the top left corner of the RMSE heatmap. As expected, scenario 3 is the most constraining one, as several parameters pairs lead to track mixing. In this situation, it is noticed that a high belief in both the model (small σ_a) and the measurements (high ρ) is required to avoid track mixing.

The RMSE can be averaged on the three scenarios, resulting in the heatmap in the right of Fig. 4. It combines the observations made for the three scenarios and features a minimum RMSE of 0.46 m for the parameter pair

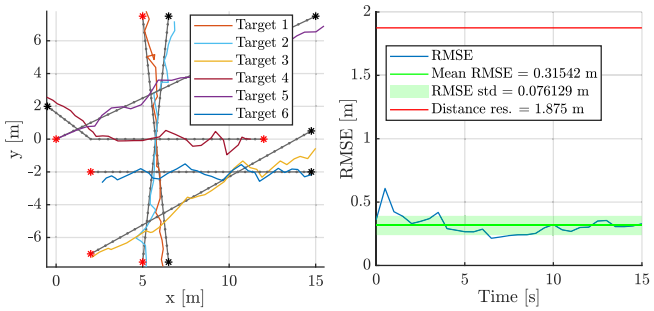

Fig. 5. Scenario 4 simulation without track management: x-y trajectory (left) and corresponding RMSE (right).

($\sigma_a = 0.6$ m/s^2, $\rho = 1$). Hence, this pair is chosen for the filter to deal with the constraints mentioned in Section V-A. By (19), the factor $\rho = 1$ means that the best tuning for the measurement error covariance matrix consists simply in taking directly the resolutions: $\boldsymbol{r} = \text{diag}(\sigma_d^2, \sigma_v^2, \sigma_\theta^2) = \text{diag}(d_{res}^2, v_{res}^2, \theta_{res}^2)$. It implies that the measurement errors are principally dictated by the radar resolutions rather than by noise.

B. RMSE Analysis for Multiple Targets

The six-target scenario is investigated with the parameters pair ($\sigma_a = 0.6$ m/s^2, $\rho = 1$) determined hereabove. The six targets are placed in a free-space area extending from 0 to 15 m along the x-axis and -10 to 10 meters in the y-axis. The targets trajectories are chosen so that parallel trajectories, target crossings and changes in trajectory occur to challenge the JPDAF-UKF. As already mentioned, RX is placed at ($x = 0, y = 0$).

1) Without Track Management: The x-y trajectories and the RMSE, along with its mean value and standard deviation, are plotted in Fig. 5 in a case without track management, *i.e.* with a fixed number of 6 tracks. On the x-y plot, grey lines correspond to the ground truth of each trajectory, while colours are used for the tracks. The start of the movement is denoted with a red star and the end of the movement with a black star.

At first, it can be noticed that the RMSE features a small peak at 0.5 s. This is due to the UKF of each target making poor estimations since it did not have the time to refine its state covariance matrix, combined with the fact that the limited range resolution causes abrupt jumps in the range measurements. These abrupt changes in range measurements also create smaller RMSE peaks later in the tracking, as noticed in the figure. A small increase of the RMSE is noticeable between the 12th and 15th seconds: this is due to the crossing of target 3 (in yellow) with target 6 (in deep blue) with a small angle between their trajectories, hence close measurements for several tracking instants, slightly confusing the JPDAF.

Overall the maximal RMSE is 0.61 m, and the mean RMSE is 0.32 m with a standard deviation of 0.08 m. This is very acceptable w.r.t. the range resolution of 1.875 m, and comparable to the 0.45 m RMSE obtained with the single target tracking in the top left of Fig. 4 with the selected parameter pair.

2) With Track Management: The same scenario is now analyzed with the track management scheme enabled,

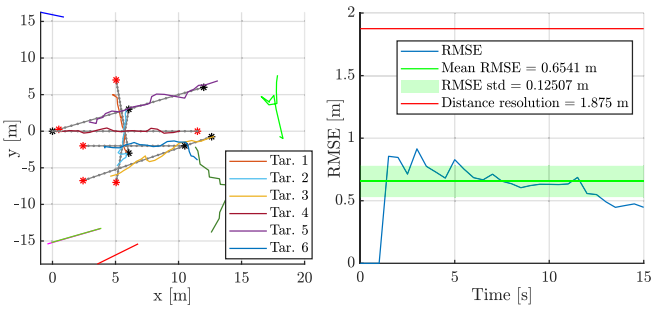

Fig. 6. Scenario 4 simulation with track management: x-y trajectory (left) and corresponding RMSE (right).

with targets appearing and disappearing at certain instants. Targets 1, 2 and 3 are appearing in the scene at 3, 5 and 5 seconds respectively and remain in it until the end of the simulation. Targets 4, 5 and 6 are present in the scene from the beginning but disappear at 10, 12 and 12 seconds respectively until the end of the simulation. Since the number of tracks is not fixed here, higher-order MPCs can give rise to ghost tracks. The validation window length is set as $N_v = 2$ for the first preliminary tracks at the initialization of the simulation and as $N_v = 3$ for the subsequent preliminary tracks. The maximal miss number is set as $N_{miss} = 2$.

The x-y trajectories of the confirmed tracks and the RMSE, along with its mean value and standard deviation, are displayed in Fig. 6. Only the tracks corresponding to targets present in the scene contribute to the RMSE at a given time instant. The delay between the appearance of a target in the scene and the confirmation of its corresponding track, due to the validation window N_v, can be noticed on the x-y plot. Similarly, the delay between the disappearance of a target in the scene and the deletion of its corresponding track, due to the maximal miss number N_{miss}, is also noticeable. Tracks that are not in the legend are false tracks initiated by ghost targets due to higher-order MPCs. They are usually deleted after a few tracking instants by the track management.

The RMSE is higher than in the case without track management. Indeed, since ghost tracks can be initiated, they affect the feasible joint association events probabilities $\mathbb{P}(A^*|\mathcal{Z})$ computed by the JPDAF through the product over tracks in (15), hence the association probabilities $\beta_{r't}$ from (16). This parasitic effect decreases the association probabilities of the correct tracks with correct measurements, *i.e.* measurements emanating from first-order MPCs from targets, degrading the performance of the tracking. Nevertheless, the mean RMSE is 0.65 m, with a standard deviation of 0.13 m, hence still significantly below the range resolution of 1.875 m and close to the 0.45 m RMSE obtained with the single target tracking in the top left of Fig. 4.

VII. Experimental Results

A. Setup

The practical performance of our Wi-Fi-based PBR is also assessed experimentally indoors. The measurements take place in a 6×20 m corridor. RX is placed at one end of the corridor, and target detection and tracking are performed assuming a known number of targets. The ground truth of the targets

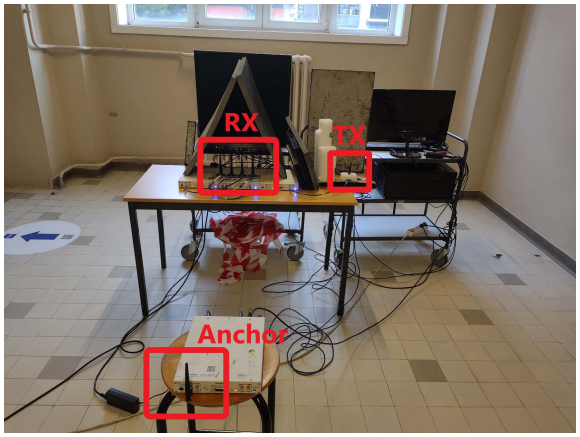

Fig. 7. Passive radar setup.

positions is determined by using markers on the ground and recording the target movements with a video camera.

Our setup consists of four USRPs X310, connected to mini helical 2.4-2.5 GHz omnidirectional antennas via Sucoflex 126E cables with SMA connectors:

- The first USRP is equipped with a single antenna and acts as TX Wi-Fi AP;
- Two USRPs are equipped each with two antennas and act as RX array. This yields the previously mentioned number of RX antennas $L = 4$;
- The last USRP is equipped with a single antenna and acts as the calibration anchor from Section III-B.

It was chosen to use a USRP as TX instead of an off-the-shelf Wi-Fi AP to have better control on the number of transmitted packets and on the time interval between bursts of packets for the experiments. The USRPs are connected via 10 Gigabit Ethernet cables to one single computer equipped with two 10Gtek X520-10G-2S-X8 10-Gigabit Ethernet cards and one 12-cores AMD Ryzen 9 3900X CPU clocked at 3.8 GHz. The Data Plane Development Kit (DPDK) [28] is used to speed up the CPU processing by manually dedicating certain cores to a specific task or entity, for example assigning one core to each USRP. The resulting processing acceleration allows the CPU to manage the anchor, TX and four RX antennas data streams simultaneously without interruptions at a rate of up to 100 Msps for each stream [29]. The clocks of TX, RX and the anchor are shared using an Octoclock CDA-2990, to avoid non-idealities such as carrier frequency offset (CFO). Clock sharing could be avoided by performing a CFO estimation with standard pilot-based techniques [13], however this is not the focus of this work. The setup is displayed in Fig. 7.

Since TX and RX are closely located, the direct TX-RX signal could cause Analog-to-Digital Converter clipping. This is avoided by tuning the amplification gains at TX and RX.

B. Scenario 1: One Target With a U-Turn

The estimated target position and the ground truth for the experimental realization of Scenario 1 are displayed on the left of Fig. 8, and the corresponding ED is displayed on the right of Fig. 8, along with its mean value and standard deviation

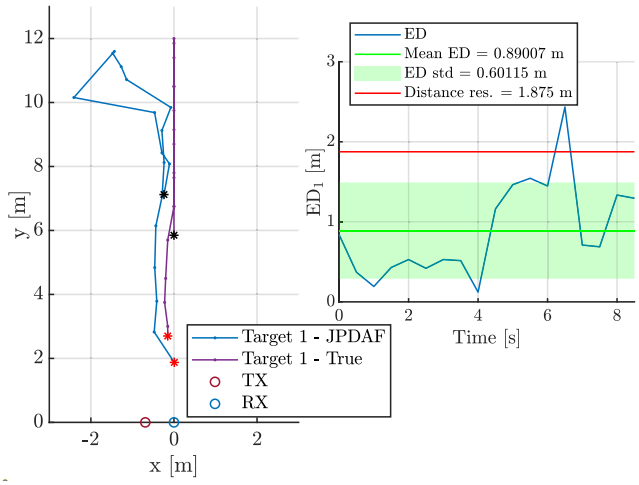

Fig. 8. Scenario 1: x-y position (left), ED (right).

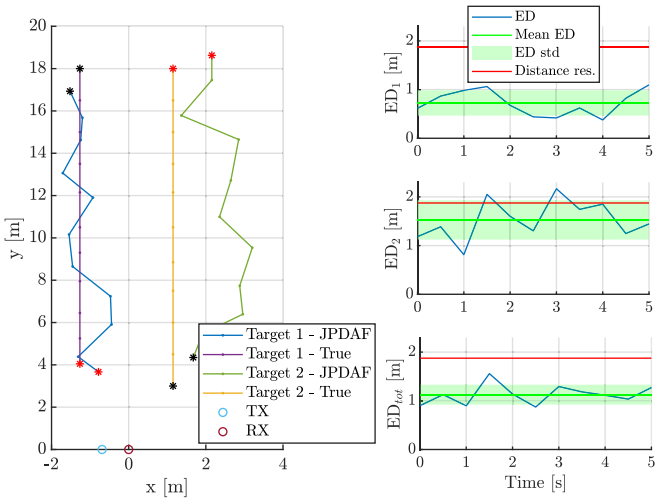

Fig. 9. Scenario 2: x-y positions (left), ED target 1 (right, top), ED target 2 (right, middle), Average ED of the 2 targets (right, bottom).

band to be compared with the range resolution. Here, the target turn around movement happens between 4.5 s and 6.5 s.

It can be seen that the ED remains at a low value, around 0.4 m, during the first part of the target movement. Then, the radar and the tracking filter manage to detect and handle the target turn around movement. As expected, this abrupt variation induces an increase in the ED. It remains inside the standard deviation region around its mean at the beginning of the turn around and then features an error peak at 6.5 s because the filter needs time to adapt the estimated state. After the adaptation time, the ED drops back to acceptable values inside the standard deviation region. So during the whole tracking, including the turn around, the ED exceeds the range resolution at only one tracking instant.

Overall, the mean ED is 0.89 m, so less than half the range resolution. It is in the order of the target size since the human target is not a point target [9]. The standard deviation is 0.60 m, so the standard deviation zone around the mean does not exceed the range resolution. This proves the efficiency of the tracking in a challenging single human target tracking case.

It has to be noted that the gating probability P_G is slightly increased from 0.99 to 0.9999 for that experiment, resulting in an increased gating region that is very sensitive to P_G, to ensure that the turn around measurement featuring a change in the speed sign is not rejected by the gating. This raises the question of assessing if JPDAF is the best data association scheme for human target tracking that can abruptly change directions. This question should be answered in future work.

C. Scenario 2: Two Targets With Opposite Speeds

For Scenario 2, the *x*-*y* trajectories are displayed in Fig. 9, along with the ED of target 1, ED of target 2, and the averaged ED on the two targets. It can be noticed that the tracking of target 2 is worse than the tracking of target 1. Indeed, target 2 starts far from RX (18 m) while target 1 starts close to RX (4 m). Hence, the target-SNR of target 2 is much lower, giving poor angle estimation. Furthermore, the impact of the angle error on position estimation increases with the distance w.r.t. the radar. Nevertheless, the mean ED of target 2 is at 1.53 m, so still below the range resolution of 1.88 m.

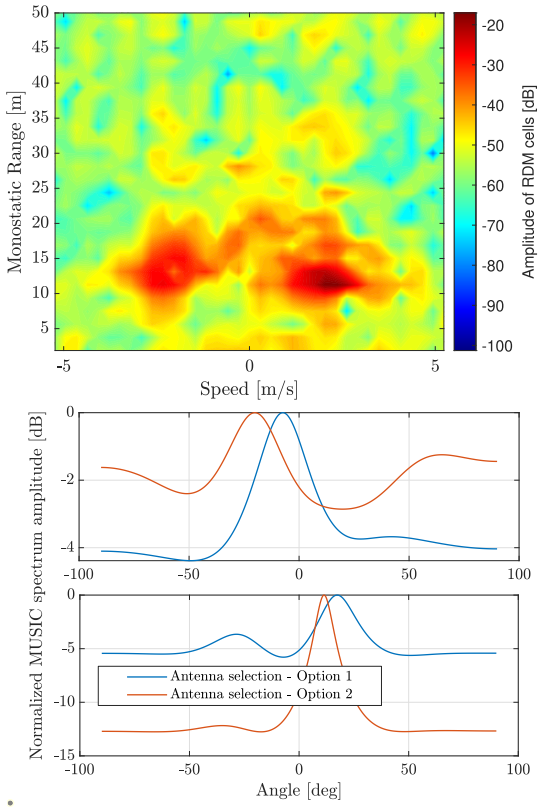

Fig. 10. Scenario 2, 6th tracking instant: RDM of the first antenna (top), MUSIC spectrum of target 1 (middle) and target 2 (bottom) with the two alternatives of the antenna selection technique.

On the other hand, the tracking of target 1 is of much better quality, yielding a mean ED of 0.73 m. Averaging the individual RSEs on the two targets and computing the mean leads to a total mean ED of 1.13 m, with a standard deviation of 0.20 m. This standard deviation is lower than both the individual standard deviations of the targets, meaning that in this case, at a given instant, when the estimated position of target 2 is poor, the estimated position of target 1 is of good

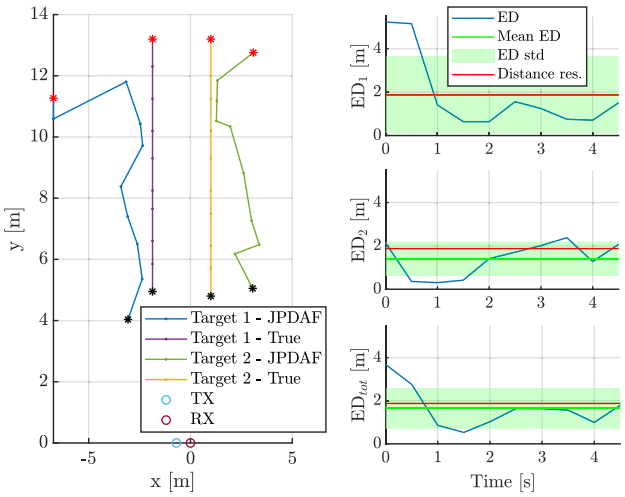

Fig. 11. Scenario 3: x-y positions (left), ED target 1 (right, top), ED target 2 (right, middle), Average ED of the 2 targets (right, bottom).

quality, keeping a stable total ED. Since the standard deviation region of the total ED is far below the range resolution, it can be concluded that the multi-target tracking is successful.

Additionally, to illustrate the intermediate steps and the radar processing, the obtained RDM at the first antenna and the MUSIC spectrum for both targets at the 6th tracking snapshot are displayed in Fig. 10. On the RDM, the two target returns can clearly be noticed: target 1 is located on the negative speed side and target 2 on the positive speed side. Each target return is surrounded by its corresponding range and speed leakage. For the angle, the antenna selection selects the option yielding the highest DR for each target, as explained in Section III-G: for target 1 the first antenna is taken as reference (option 1, blue curve), yielding a MUSIC spectrum peak at $-7.4°$, while the ground truth is $-6.9°$. The error on the angle is thus negligible in this case. For target 2, separate antennas detections are used (option 2, orange curve), yielding a MUSIC spectrum peak at 17.4°, while the ground truth is 6.25°. This large error can be explained by a misdetection on the 4th antenna.

D. Scenario 3: Two Targets Moving Side-by-Side

The *x*-*y* trajectories and the EDs of Scenario 3 are displayed in Fig. 11. It can be noticed that the tracking is more difficult than in the previous case. Indeed, when the targets start their movement at a far distance, their target-SNR is small and their difference in angle is less than 15 degrees. Therefore, with a four-antenna receiver, the two targets cannot be resolved in the MUSIC spectrum without large errors. Hence, the track initialization is far from the ground truth, giving a large ED, especially for target 1 in this case. Furthermore, since the distance between the measurements originating from the two targets is small in the measurement domain, the JPDAF has difficulties discriminating the measurements origin and hence attributes weights of close value to the measurements, meaning that target 1 heavily influences target 2 and vice-versa.

However, after a few tracking instants, the filter manages to recover and the track gets closer to the ground truth, causing the ED to go below the range resolution. On average, the mean ED of target 1 is very close to the range resolution, and the mean ED of target 2 is 1.41 m, so slightly below the range resolution. In total, the averaged ED of the two targets has a mean value of 1.65 m and a standard deviation of 0.95 m. The total mean ED is thus slightly below the range resolution but this clearly shows that the multi-tracking is here pushed to its limits due to the poor separation of the targets in the measurement space combined with weak target-SNR.

VIII. Conclusion

We demonstrated the feasibility of an indoor human multi-target tracking based on a JPDAF-UKF using a Wi-Fi-based multi-antenna PBR leveraging the Preamble of the packets of the latest Wi-Fi standard, 802.11ax. We built a prototype using USRPs, featuring an over-the-air calibration and automatic reference antenna selection, and resorting to CPU acceleration to handle several data streams with a high sampling rate. Simulations were performed to fine-tune the UKF parameters and to assess the performance of the tracking with a high number of targets. The real-life performance of the tracking was also tested on three measurements scenarios, showing that it successfully deals with constraints such as the limited range resolution and the slow tracking time, even at long distances. The tracking performance was benchmarked for an extremely challenging scenario, *e.g.*, when two targets are consistently closer than the range resolution and moving in the same direction and speed. Our proposed scheme features a larger error in such a scenario, but still under the range resolution.

References

[1] IEEE 802.11. (2021). *Wi-Fi Sensing*. Accessed: Feb. 2021. [Online]. Available: https://www.ieee802.org/11/Reports/tgbf_update.htm

[2] P. Falcone, F. Colone, and P. Lombardo, "Potentialities and challenges of WiFi-based passive radar," *IEEE Aerosp. Electron. Syst. Mag.*, vol. 27, no. 11, pp. 15–26, Nov. 2012.

[3] B. Tan, K. Woodbridge, and K. Chetty, "A wireless passive radar system for real-time through-wall movement detection," *IEEE Trans. Aerosp. Electron. Syst.*, vol. 52, no. 5, pp. 2596–2603, Oct. 2016.

[4] P. Falcone *et al.*, "Active and passive radar sensors for airport security," in *Proc. Tyrrhenian Workshop Adv. Radar Remote Sens.*, Sep. 2012, pp. 314–321.

[5] Aruba Networks. (2019). *White Paper: 802.11ax*. Accessed: Feb. 2020. [Online]. Available: https://www.arubanetworks.com/assets/wp/WP_802.11AX.pdf

[6] L. Storrer, H. C. Yildirim, C. Desset, M. Bauduin, A. Bourdoux, and F. Horlin, "Clutter removal for Wi-Fi-based passive bistatic radar," in *Proc. IEEE 91st Veh. Technol. Conf. (VTC-Spring)*, May 2020, pp. 1–5.

[7] H. C. Yildirim, L. Storrer, M. V. Eechkhaute, C. Desset, J. Louveaux, and F. Horlin, "Passive radar based on 802.11ac signals for indoor object detection," in *Proc. 16th Eur. Radar Conf. (EuRAD)*, 2019, pp. 153–156.

[8] L. Storrer *et al.*, "Experimental implementation of a multi-antenna 802.11 ax-based passive bistatic radar for human target detection," in *Proc. IEEE Radar Conf. (RadarConf)*, Sep. 2020, pp. 1–6.

[9] P. Falcone, F. Colone, A. Macera, and P. Lombardo, "Two-dimensional location of moving targets within local areas using WiFi-based multistatic passive radar," *IET Radar, Sonar Navigat.*, vol. 8, no. 2, pp. 123–131, Feb. 2014.

[10] P. Falcone, F. Colone, A. Macera, and P. Lombardo, "Localization and tracking of moving targets with WiFi-based passive radar," in *Proc. IEEE Radar Conf.*, May 2012, pp. 705–709.

[11] Q. Chen, B. Tan, K. Woodbridge, and K. Chetty, "Indoor target tracking using high Doppler resolution passive Wi-Fi radar," in *Proc. IEEE Int. Conf. Acoust., Speech Signal Process. (ICASSP)*, Apr. 2015, pp. 5565–5569.

[12] M. Broetje, "Person tracking for WiFi based multistatic passive radar," in *Proc. 16th Int. Conf. Inf. Fusion*, 2013, pp. 280–287.
[13] Y. S. Cho, J. Kim, W. Y. Yang, and C. G. Kang, *MIMO-OFDM Wireless Communications With MATLAB*. Hoboken, NJ, USA: Wiley, 2010.
[14] M. Richards, W. Holm, and J. Scheer, *Principles of Modern Radar: Basic Principles* (Electromagnetics and Radar). Edison, NJ, USA: IET, 2010. [Online]. Available: https://books.google.be/books?id=nD7tGAAACAAJ
[15] J. G. Proakis, M. Salehi, N. Zhou, and X. Li, *Communication Systems Engineering*, vol. 2. Upper Saddle River, NJ, USA: Prentice-Hall, 1994.
[16] D. Jenn, "Radar fundamentals," *Dept. Elect. Comput. Eng.*, vol. 93943, p. 831, 2007.
[17] M. Jokinen, M. Sonkki, and E. Salonen, "Phased antenna array implementation with USRP," in *Proc. IEEE Globecom Workshops (GC Wkshps)*, Dec. 2017, pp. 1–5.
[18] R. O. Schmidt, "Multiple emitter location and signal parameter estimation," *IEEE Trans. Antennas Propag.*, vol. AP-34, no. 3, pp. 276–280, Mar. 1986.
[19] S. J. Julier and J. K. Uhlmann, "New extension of the Kalman filter to nonlinear systems," in *Proc. 6th Signal Process., Sensor Fusion, Target Recognit.*, vol. 3068. Orlando, FL, USA: International Society for Optics and Photonics, 1997, pp. 182–193.
[20] R. Labbe, "Kalman and Bayesian filters in Python," *Chap*, vol. 7, no. 246, p. 4, 2014.
[21] E. I. P. Copa, K. Aziz, M. Rykunov, E. De Greef, A. Bourdoux, and F. Horlin, "Radar fusion for multipath mitigation in indoor environments," in *Proc. IEEE Radar Conf. (RadarConf)*, Sep. 2020, pp. 1–5.
[22] Y. Bar-Shalom, F. Daum, and J. Huang, "The probabilistic data association filter," *IEEE Control Syst.*, vol. 29, no. 6, pp. 82–100, Dec. 2009.
[23] G. Grisetti, C. Stachniss, K. Arras, and W. Burgard, "Robotics data association," Univ. Freiburg, Breisgau, Germany, 2010.
[24] C. Qiu, Z. Zhang, H. Lu, and H. Luo, "A survey of motion-based multitarget tracking methods," *Prog. Electromagn. Res. B*, vol. 62, pp. 195–223, Mar. 2015. [Online]. Available: https://www.jpier.org/PIERB/pier.php?volume=62
[25] Y. Bar-Shalom and X.-R. Li, *Multitarget-Multisensor Tracking: Principles and Techniques*, vol. 19. Storrs, CT, USA: YBS, 1995.
[26] B. Vandersmissen *et al.*, "Indoor person identification using a low-power FMCW radar," *IEEE Trans. Geosci. Remote Sens.*, vol. 56, no. 7, pp. 3941–3952, Jul. 2018.
[27] S. Monfared, T.-H. Nguyen, T. Van der Vorst, P. De Doncker, and F. Horlin, "Experimental demonstration of AoA estimation uncertainty for IoT sensor networks," in *Proc. IEEE VTC Spring*, May 2020, pp. 1–5.
[28] The Linux Foundation Project. (2021). *Data Plane Development Kit*. Accessed: Feb. 2021. [Online]. Available: https://www.dpdk.org
[29] H. C. Yildirim *et al.*, "Super resolution passive radars based on 802.11ax Wi-Fi signals for human movement detection," *IET Radar, Sonar Navigat.*, vol. 15, no. 4, pp. 323–339, Apr. 2021.

Laurent Storrer (Member, IEEE) received the M.Sc. degree in electrical engineering from the Université Libre de Bruxelles (ULB), Brussels, Belgium, and the Vrije Universiteit Brussel (VUB) in 2019.

He is working on Wi-Fi-based passive radars, target tracking and classification for crowd monitoring. In 2016, he received a Scholarship of Initiation to Research from ULB to perform research on multi-criteria decision aid. In 2019, he carried out an internship at IMEC on Wi-Fi-based sensing. He is currently a Ph.D. Researcher jointly at ULB and at KU Leuven with a scholarship from F.N.R.S.–E.O.S.

Hasan Can Yildirim (Member, IEEE) was born in Turkey, in 1991. He received the M.Sc. degree in electrical engineering from ULB and VUB. He is pursuing the Ph.D. degree with the OPERA Department, with a scholarship from F.N.R.S.–F.R.I.A. He is working on passive radars-based on emerging Wi-Fi systems.

Morgane Crauwels received the B.Sc. degree in electrical engineering from ULB in 2018, and the M.Sc. degree in electrical engineering from ULB and VUB in 2020. She is a Belgian Electrical Engineer. She is working with the Hubgrade Smart monitoring Center of Veolia, Brussels.

Evert I. Pocoma Copa was born in El Alto, Bolivia, in 1990. He received the M.Sc. degree in electrical engineering from ULB & VUB in 2019, through a Scholarship from the Foundation Simon I. Patiño. He is pursuing the Ph.D. degree with the OPERA-WCG, ULB. He is currently working on distributed localization and tracking techniques in wireless sensor networks.

Sofie Pollin (Senior Member, IEEE) received the Ph.D. (Hons.) degree from KU Leuven in 2006. From 2006 to 2008, she continued her research on wireless communication, energy-efficient networks, cross-layer design, coexistence, and cognitive radio with UC Berkeley. In November 2008, she returned to imec to become a Principal Scientist with the Green Radio Team. She is an Associate Professor with the Electrical Engineering Department, KU Leuven. Her research interest includes constrained networked systems.

Jérôme Louveaux (Member, IEEE) received the degree in electrical engineering and the Ph.D. degree from the Université Catholique de Louvain (UCL), Louvain-la-Neuve, Belgium, in 1996 and 2000, respectively. From 2000 to 2001, he was a Visiting Scholar with the Electrical Engineering Department, Stanford University, Stanford, CA, USA. From 2004 to 2005, he was a Postdoctoral Researcher with the Delft University of Technology, The Netherlands. Since 2006, he has been a Professor with the ICTEAM Institute, UCL. His research interests include signal processing for digital communications, and in particular: multicarrier modulations, xDSL systems, resource allocation, synchronization, and estimation.

Philippe De Doncker (Member, IEEE) received the M.Sc. degree in physics engineering and the Ph.D. degree in science engineering from ULB in 1996 and 2001, respectively. He is currently a Professor with ULB, where he also leads the research activities on wireless channel modeling and electromagnetics.

François Horlin (Member, IEEE) received the Ph.D. degree from UCL in 2002. He specialized in the field of signal processing for digital communications. His Ph.D. research aimed at optimizing the multi-access for 3G cellular communications. He joined the Inter-university Micro-Electronics Center (IMEC), as a Senior Scientist, in 2006. He became a Professor with the Université libre de Bruxelles (ULB) in 2007. He is supervising a research team working on modern communication systems. Recently, the team focused on the design of Wi-Fi-based passive radars for crowd monitoring.